Am J Transl Res 2025;17(1):162-177
www.ajtr.org /ISSN:1943-8141/AJTR0157190

Original Article

Delta/pre-radiomics based on enhanced CT predicts complete response in locally advanced esophageal squamous cell carcinoma

Yan Zhu[1,3], Zhenzhong Zhang[2], Genji Bai[3], Lili Guo[3], Qingqing Xu[3], Lili Zhang[4], Yiping Gao[1], Shuangqing Chen[1]

[1]Department of Radiology, The Affiliated Suzhou Hospital of Nanjing Medical University, Suzhou Municipal Hospital, Gusu School, Nanjing Medical University, Suzhou, Jiangsu, China; [2]Deparment of Cardiothoracic Surgery, The Affiliated Huaian No. 1 People's Hospital of Nanjing Medical University, Huai'an, Jiangsu, China; [3]Deparment of Medical Imaging Center, The Affiliated Huaian No. 1 People's Hospital of Nanjing Medical University, Huai'an, Jiangsu, China; [4]Deparment of Pathology, The Affiliated Huaian No. 1 People's Hospital of Nanjing Medical University, Huai'an, Jiangsu, China

Received August 29, 2024; Accepted December 2, 2024; Epub January 15, 2025; Published January 30, 2025

Abstract: Objectives: This study aimed to evaluate the effectiveness of neoadjuvant immunochemotherapy (NIC) in patients diagnosed with locally advanced esophageal squamous cell carcinoma (LAESCC), by assessing the performance of models that utilize enhanced computed tomography (CT) images at the pre, post, and delta/pre group stages. Methods: A total of 225 patients were included in our study and randomly divided into a training set (n = 157) and test set I (n = 68). In addition, we conducted a test set II involving 60 patients from another center. We obtained omics features from CT images before and after NIC. Then, the delta radiomics features were obtained by calculating the differences between the post and pre group features, which was then divided by the pre group features to obtain the delta/pre group. Imaging and clinicopathological data were collected in the two centers according to the same inclusion and exclusion criteria. The tumor regression grading (TRG) system was used according to the Japanese Esophageal Cancer (11th edition). Three sets of models were built and their performance was assessed using receiver operating characteristic (ROC) curve, confusion matrix, and calibration curve. The clinical utility of the model was evaluated through decision curve analysis and nomogram. Results: The area under the curve value of the delta/pre-radiomics (Rad) score model was 0.876 in the training set and 0.827 and 0.749 in the two test sets, which was significantly higher than that in the pre and post Rad score models. The radiomics nomogram was constructed using Rad scores derived from the post model, delta/pre model, Ki67, P53, and the pathological stage of lymph node after neoadjuvant therapy (ypN), demonstrating robust performance. The internal correction curve (apparent) and the external correction curve (bias-corrected) exhibited negligible deviations from the ideal curve, thereby demonstrating a high level of similarity. Conclusion: Nomogram, based on delta/pre-enhanced CT features and clinical risk indicators, is a non-invasive tool to predict therapeutic effects in patients with LAESCC after NIC.

Keywords: Locally advanced esophageal squamous cell carcinoma, delt radiomics, neoadjuvant immunochemotherapy, pathological complete response, prediction model

Introduction

Approximately 90% of esophageal squamous cell carcinomas (ESCC) occur in East Asia, with approximately 50% of cases concentrated in China, particularly in the provinces of Henan, Hebei, and Jiangsu. Of these ESCCs, 50% are diagnosed at an advanced local stage [1]. According to the National Comprehensive Cancer Network (NCCN) guidelines, neoadjuvant chemoradiotherapy (nCRT) followed by radical surgery has emerged as an alternative treatment for locally advanced ESCC (LAESCC) [2]. Although neoadjuvant therapy has demonstrated improved overall survival rates in patients with LAESCC, the increased surgical complexity associated with neoadjuvant chemotherapy and chemoradiotherapy remains a concern [3]. Since 2018, multiple clinical studies have reported improved overall survival

https://doi.org/10.62347/WQYO9624

rates with the application of new adjuvant immunotherapies combined with chemotherapy (NIC) in patients with ESCC, as they can achieve higher pathological and morphological tumor regression grading [4]. Currently, NIC combined with radical surgery is emerging as the first-line treatment for advanced ESCC in China, Japan, and South Korea [5, 6]. According to previous clinical studies, the complete pathological response rate of patients undergoing nRCT was 29.9%, whereas that of patients receiving NIC was 58.3% [7]. However, visual assessment of NIC in LAESCC remains challenging. With advancements in research, scientists have increasingly recognized that tumors exhibit changes in response to treatment, and evaluating the distribution of intratumoral heterogeneity can provide valuable insights into tumor characteristics during treatment [8]. Consequently, conventional imaging diagnoses have become inadequate to meet clinical demands. Thus, more studies have focused on radiomics analysis. Previous studies have demonstrated that imaging features can assist in quantifying microenvironmental changes within tumor tissues following NIC treatment, thereby enabling the evaluation of the extent of tumor regression and ultimately assessing the efficacy of NIC for LAESCC [9]. Delta radiomics refers to temporal changes in radiomic features, comprehensively reflecting tumor characteristics pre- and post-treatment. We compared the performance of a pre- and post-neoadjuvant CT-enhanced image feature model, a delta/pre-feature model, and a machine learning model incorporating clinical indicators to assess the predictive efficacy of NIC in patients with LAESCC. The tumor regression grading system is based on the degree of therapeutic fibrosis associated with the residual tumors. This study focused on postoperative TRG in patients with LAESCC who underwent NIC and we aimed to identify the risk factors associated with the combination of NIC by analyzing clinical and hematological biochemical indicators.

Furthermore, imaging methods were employed to extract pre- and post-NIC imaging features of LAESCC. By incorporating delta/pre-radiomic features, a predictive model based on enhanced CT imaging was developed to assess NIC efficacy [10]. This model enabled the preliminary evaluation of NIC efficacy and provided valuable insights for informed decision-making.

Materials and methods

Patients

A retrospective analysis was performed on 225 consecutive patients in the Affiliated Huai'an No. 1 Hospital of Nanjing Medical University (A hospital). In addition, a retrospective review of 60 patients was conducted at the Affiliated Suzhou Hospital of Nanjing Medical University (B hospital). Ultimately, 225 patients from hospital A were enrolled and randomly assigned to the training set (n = 157) and test set I (n = 68) with a split ratio of 7:3, whereas patients from hospital B constituted the external set (test set II, n = 60). All patients diagnosed with cT3 or cT4 ESCC without distant organ metastasis, who underwent NIC followed by radical surgery between January 2019 and April 2024, were included in this study. An experienced thoracic surgeon and radiologist assessed the patients with histologically confirmed cT3 or cT4 ESCC based on gastroscopy findings and enhanced CT images. This analysis was conducted after obtaining approval from the institutional review board (Approval No: KY-2022-045-01).

The patient selection criteria were as follows: 1) confirmation of ESCC through pre-treatment gastroscopy; 2) pre- and post-NIC enhanced CT examinations of the neck, chest, and upper abdomen for all patients; 3) absence of distant organ metastasis or other tumors; 4) administration of neoadjuvant chemotherapy combined with immunotherapy for a duration ranging from one to four cycles in all patients; 5) assessment of TRG after surgery; 6) immunohistochemistry analysis performed on all postoperative pathologies. The same patient selection criteria were applied to the external validation set.

Although esophageal cancer may predominantly manifests as adenocarcinoma in Caucasian patients, this may not directly apply to individuals of Asian descent [10, 11]. Therefore, this study determined the tumor regression grade after NIC treatment according to the Japanese Esophageal Cancer (11th edition) as follows [12]: Grade 3, no viable tumor cells remaining; Grade 2, active tumor cells < 1/3 of the tumor site, with some cancer cell degeneration or necrosis; Grade 1b, active tumor cells > 1/3 of the tumor site but < 2/3; Grade 1a, active

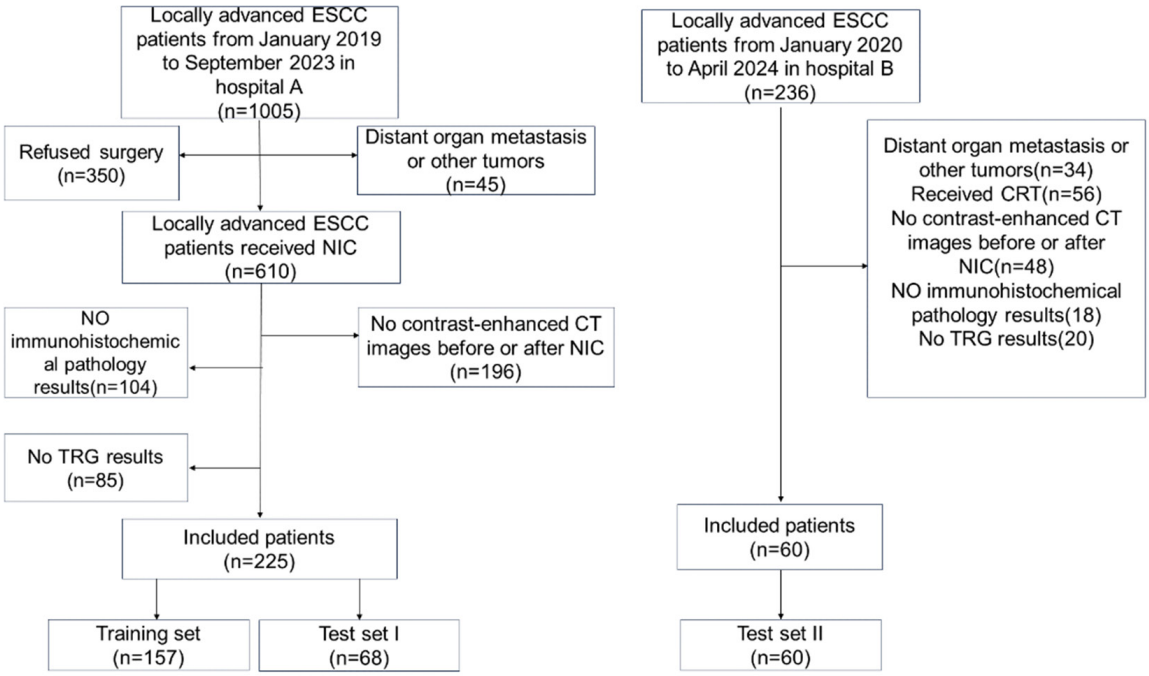

Figure 1. Flow chart illustrating the pathway for recruiting patients.

tumor cells > 2/3 of the tumor site. Patients with ESCC were stratified based on their response to NIC treatment, with grades 3 and 2 categorized as Group 1 (good responders) and grades 1a and 1b divided into Group 2 (poor responders). A pathologist with extensive experience established the classification and diagnosis.

All the patients provided written informed consent for the selected treatments. We assessed neoadjuvant therapy toxicity based on the guidelines outlined in the National Cancer Institute Common Terminology Criteria for Adverse Events version 5.0. **Figure 1** shows the study flowchart.

Clinical characteristics

The information on clinical and immunohistochemical indicators was extracted from the electronic medical records and compared between good and poor responders in the training set, test set I, and test set II. These indicators included age, sex, long tumor diameter, number of lymph nodes after NIC, ypN, R0 resection status (R0), keratin expression level (Ker), lymphatic vessel invasion (LVI), Ki67 expression level (Ki67), and P53 mutation status (P53).

Ker and LVI were determined based on immunohistochemical results, with positive results recorded as 1 and negative results as 0. Ki67 overexpression (> 70%) was recorded as 1, while Ki67 non-expression and low expression (≤ 70%) were recorded as 0. P53 overexpression (≥ 40%) was defined as 1, and P53 negative or low expression (0%-39%) was defined as 0 [13].

CT acquisition

All patients underwent CT-enhanced examination before and after NIC to ensure consistency in the tumor length along the sagittal plane. CT images of each patient were obtained pre- and post-NIC to confirm that the tumor maintained its original dimensions. The post-NIC target area was referenced from the pre-NIC target area to ensure an accurate comparison. An experienced radiologist measured the tumor length. The CT parameters used in Hospitals A and B are presented in Supplementary Material 1.

NIC regimen and esophagectomy

A total of 225 patients (Hospital A) received one to four cycles of immunochemotherapy (APC regimens): albumin-bound paclitaxel,

nedaplatin (APC) and camrelizumab. Sixty patients (Hospital B) received one to four cycles of immunochemotherapy (NAC-DCF regimens): docetaxel plus cisplatin and 5-FU (NAC-DCF) and nivolumab. Each course of medication was administered for 1-4 days. Minimally invasive thoracoscopic radical surgery was performed 3-4 weeks after completing the last cycle.

Radiomics feature extraction

An experienced radiologist and seasoned thoracic surgeon delineated the region of interest (ROI) of the lesion semi-manually on ITKsnap (version 4.0.1, http://www.itksnap.org/pmwiki/pmwiki.php). The ROI contained all tumors, avoiding lesional gas. First, an outline of the tumor was drawn on enhanced CT images before NIC. The ROI after NIC was continually elucidated by referring to the ROI before NIC. Thus, the target area before and after the treatment remained unchanged. A chief radiologist reviewed the mapped lesions. **Figure 2** illustrates the radiomics flowchart.

Radiomics feature selection and rad-score development

In this study, the PyRadiomics open-source package (version 3.1.0) was used to extract CT image features from the pre-, post-, and delta/pre-groups. Next, we preliminarily cleaned the data of the three groups and used the z-score function to non-dimensionalize the data. Then, a nonlinear support vector machine (SVM) was used to evaluate the importance of the features, utilizing five cross-validations repeated five times to obtain the alpha with the root mean square error. We selected the top 20 features based on their important scores. In addition, a recursive feature elimination (RFE) algorithm removed unimportant features. We retrained the model on the remaining features and repeated the step five times until reaching the desired number of features and returning the final selected optimal feature subset. This method was simple and easily understood without setting complex parameters, but it required a considerable amount of time for calculation and necessitated repeated model training, which increased the risk of overfit and lead to degraded model performance. Therefore, it is necessary to select the number of features manually to set the recursive-end condition. The detailed steps for Radiomics feature selection are provided in Supplmentary Matetrial 3. A RAD-score was formulated using a logistic regression combination of these features in the three groups, each given its respective coefficient.

$$\text{Log it}(P) = \alpha + \beta 1\, x1 + \beta 2\, x2 + \ldots\ldots \beta n x n.$$

The specific derivation equation is available in Supplementary Material 2.

Statistical analysis

Statistical analyses were performed using PyCharm (Python version 3.13.1) and R software (version 3.6.3). Continuous variables are described using the mean ± standard deviation (SD), while categorical variables are described using frequencies and percentages. Comparisons between Group 1 (PCR) and Group 2 (no-PCR) were conducted using independent-sample t-tests or Mann-Whitney U tests for continuous variables and the chi-square test for binary or categorical variables. The Fisher's exact test was used when the frequency was < 5. ROC curves were plotted for each model, and the performance of the models was evaluated using AUC values, along with the confusion matrix. We also assessed the predictive performance of each model using tests set 1 and 2. Calibration and clinical decision curves were plotted for models exhibiting superior AUC performance to guide clinical decision-making. Additionally, we constructed nomograms using radar features combined with clinicopathological indicators.

Results

Patient characteristics

The clinicopathological indicators of patients are shown in **Table 1**. The effectiveness of NIC in patients with LAESCC significantly correlated with Ki67, LVI, and ypN levels ($P < 0.05$). This correlation was confirmed in training and test sets I and II. Significant differences were observed in the R0 resection rates and P53 status between the training set and test set I; however, these findings were not validated in test set II ($P = 0.025$ vs. $P = 0.228$). Moreover, significant differences were found in perineural invasion (PNI) and lymph node counts between the training set and test set II but not in test set I ($P = 0.239$ vs. $P = 0.073$). Other

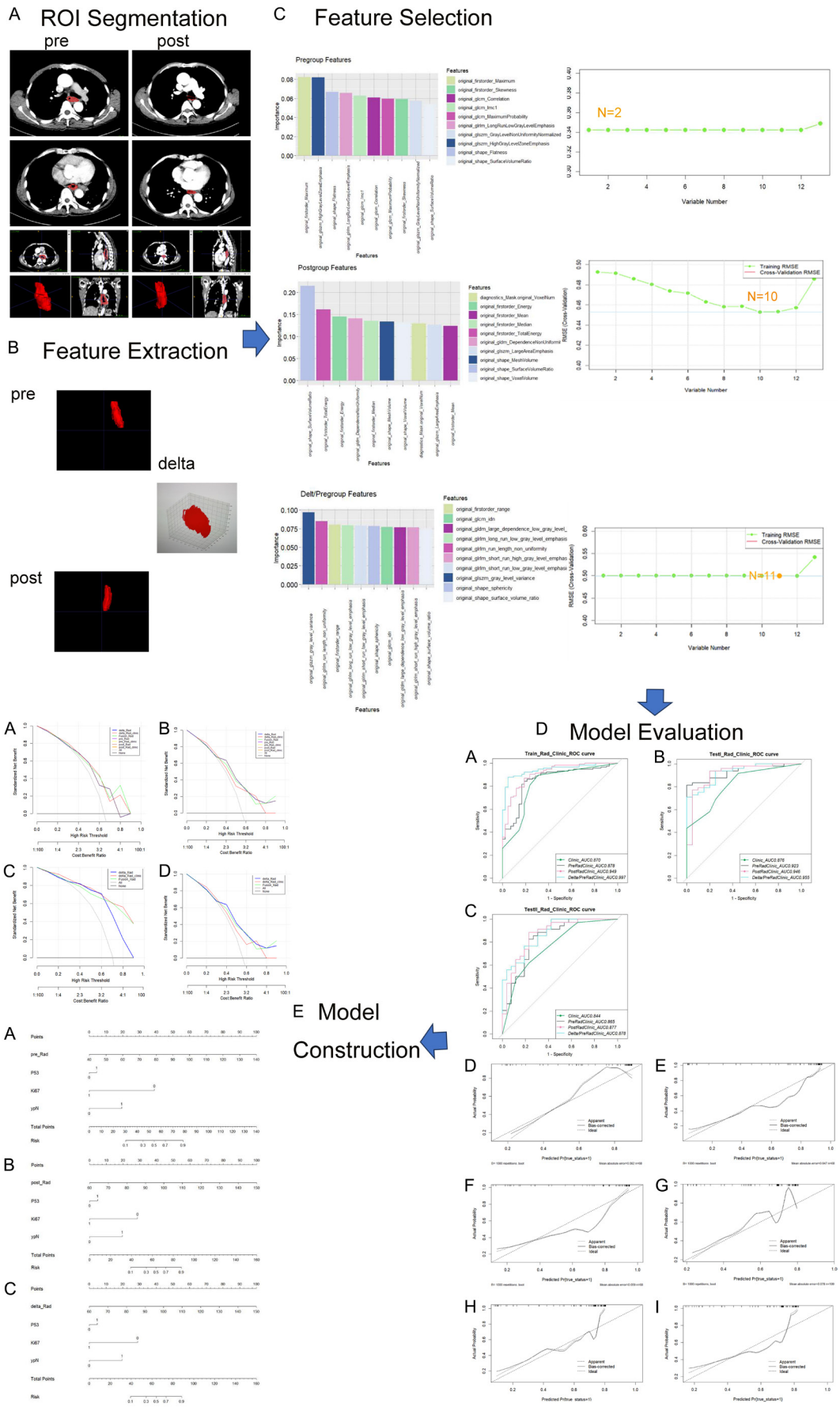
A ROI Segmentation
pre
post
B Feature Extraction
pre
delta
post
C Feature Selection
Pregroup Features
N=2
Postgroup Features
N=10
Delt/Pregroup Features
N=11
Training RMSE
Cross-Validation RMSE
Variable Number
D Model Evaluation
E Model Construction

Figure 2. Work flow chart of feature screening.

Table 1. Clinical features of patients in the training set, test set I and test set II

Features	Train set			Test set I			Test set II		
	Group 1 n = 42	Group 2 n = 115	P	Group 1 n = 20	Group 2 n = 48	P	Group 1 n = 26	Group 2 n = 34	P
Age, year			.695			.664			.692
Mean±SD	65.10±6.45	66.33±6.38		62.70±5.75	66.48±6.09		65.73±8.09	65.35±7.07	
Sex (%)			.408			.782			.896
Male	29 (69.0%)	88 (76.5%)		13 (65.0%)	33 (68.8%)		21 (80.8%)	27 (79.4%)	
Female	13 (31.0%)	27 (23.5%)		7 (35.0%)	15 (31.2%)		5 (19.2%)	7 (20.6%)	
R0-section (%)			.000*			.000*			.025*
Yes	42 (100%)	50 (43.5%)		20 (100.0%)	24 (50.0%)		22 (84.6%)	19 (55.9%)	
No	0 (0%)	65 (56.5%)		0 (0%)	24 (50.0%)		4 (15.4%)	15 (44.1%)	
Ker (%)			.000			.079*			0.076*
Yes	34 (81.0%)	55 (47.8%)			18 (90.0%)	34 (70.8%)	21 (80.8%)	33 (97.1%)	
No	8 (19.0%)	60 (52.2%)			2 (10.0%)	14 (29.2%)	5 (19.2%)	1 (2.9%)	
Lvi (%)			.001*			.050*			.0126*
Yes	42 (100.0%)	95 (82.6%)		20 (100.0%)	40 (83.3%)		26 (100%)	30 (88.2%)	
No	0 (0%)	20 (17.4%)		0 (0%)	8 (16.7%)		0 (0%)	4 (11.8%)	
PNI (%)			.000*			.239*			.016*
Yes	42 (100.0%)	98 (85.2%)		20 (100.0%)	44 (91.7%)		25 (96.2%)	24 (70.6%)	
No	0 (0%)	17 (14.8%)		0 (0%)	4 (8.3%)		1 (3.8%)	10 (29.4%)	
Ki67 (%)			.000*			.000*			.003*
Yes	39 (92.9%)	64 (55.7%)		19 (95.0%)	24 (50.0%)		16 (61.5%)	32 (94.1%)	
No	3 (7.1%)	51 (44.3%)		1 (5.0%)	24 (50.0%)		10 (38.5%)	2 (5.9%)	
P53 (%)			.000*			.001*			.028*
Yes	38 (90.5%)	51 (44.3%)		16 (80.0%)	18 (37.5%)		22 (84.6%)	23 (67.6%)	
No	4 (9.5%)	64 (55.7%)		4 (20.0%)	30 (62.5%)		4 (15.4%)	11 (32.4%)	
ypN (%)			.000			0.028			.007*
N-0	34 (81.0%)	56 (48.7%)		14 (70.0%)	26 (54.2%)		22 (84.6%)	17 (50.0%)	
N-I-II	8 (19.0%)	59 (51.3%)		6 (30.0%)	22 (45.8%)		4 (15.4%)	17 (50.0%)	
N-counts			.002			.073			.000
Mean±SD	0.36±0.85	1.31±0.226		0.45±0.826	1.02±1.604		0.15±0.368	1.60±2.271	
Pre_Rad									
Mean±SD	21.64±7.21	25.6±13.25	0.064	18.83±4.58	24.32±8.63	0.009	53.66±9.08	61.8±17.69	0.035
Post_Rad									
Mean±SD	188.5±0.71	190.7±2.71	0.000	188.60±1.10	190.4±2.58	0.001	87.0±10.03	99.8±17.21	0.001
Delt/Pre_Rad									
Mean±SD	75.17±5.70	83.3±13.46	0.000	75.34±5.01	82.21±7.77	0.001	87.1±10.18	99.98±17.6	0.001

R0: resection status; Ker: Keratin expression level; LVI: lymphatic vessel invasion; Ki67: Ki67 expression level; P53: P53 mutation status; ypN: lymph node after neoadjuvant therapy; Rad: radiomics; PNI: perineural invasion. *: it means the *P* value is less than 0.05.

clinical indicators were not significantly different across the three datasets.

Radiomics features screening

The omics image features were derived from the pre- and post-group datasets obtained from Hospitals A and B. To calculate the delta, the difference between the pre- and post-groups was divided by the pre group, resulting in a new feature set called delta/pre group. Radiomics features with an intraclass correlation coefficient (ICC) < 0.8 were excluded from the pre-, post-, and delta/pre-group datasets.

This study extended the RFE algorithm to rank variables based on a nonlinear (polynomial, radial, and sigmoid) SVM. We identified the most relevant predictor variables by selecting the best-performing kernel function for each RFE iteration and visually represented it, then we selected the top 20 ranked variables. Subsequently, we assessed the three methods

Table 2. Extracted radiomic features

PreGroup	PostGroup	Delta/PreGroup
original_shape_Flatness	original_shape_SurfaceVolumeRatio	original_glszm_gray_level_variance
original_firstorder_Maximum	original_firstorder_TotalEnergy	original_firstorder_range
	original_firstorder_Energy	original_glrlm_long_run_low_gray_level_emphasis
	original_firstorder_Median	original_gldm_large_dependence_low_gray_level_emphasis
	original_shape_MeshVolume	original_shape_sphericity
	original_shape_VoxelVolume	original_gldm_small_dependence_low_gray_level_emphasis
	original_firstorder_Mean	original_gldm_small_dependence_low_gray_level_emphasis
	diagnostics_Mask_original_VoxelNum	original_glszm_high_gray_level_zone_emphasis
	original_shape_Sphericity	original_glrlm_short_run_high_gray_level_emphasis
	original_glszm_LargeAreaEmphasis	original_glrlm_short_run_high_gray_level_emphasis
		original_glcm_imc1

by employing pseudo-samples and kernel principal component analysis and compared their performance with that of the original SVM-RFE algorithm.

Finally, the model was retrained using the top 20 features, and a 5-fold cross-validation technique was employed to identify the optimal feature subset to ensure superior performance. Specifically, we retained 2, 11, and 10 features for the pre-, post-, and delta/pre-groups, respectively. The results are summarized in **Table 2**.

Rad-score building based on radiomic features

All coefficients in the equation were determined using lasso-logistic regression analysis conducted using R software. The ranges of the pre-group Rad scores were as follows: training set: pre-group (4.912-89.680); post-group (187.344-204.396); delta/pre-group (59.522-176.876); test set I: pre-group (8.131-49.678); post-group (186.045-203.970); delta/pre-group (65.920-101.021); test set II: pre-group (43.540-137.181), post-group (68.564-148.363), delta/pre-group (68.310-148.682). Tumor aggressiveness was evaluated further using Rad scores to establish a predictive model. ROC curve analysis demonstrated that the Rad score exhibited moderate predictive efficacy for the PCR and no-PCR groups.

The respective AUCs of the three models were 0.577, 0.762, and 0.876 in the training set (**Figure 3A**), 0.707, 0.762, and 0.827 in test set I (**Figure 3B**), and 0.729, 0.748, and 0.749 in test set II (**Figure 3C**). **Table 3** presents the accuracy rates along with the sensitivity and specificity values for each radiomic model at a confidence interval of 95%. The experimental findings indicate that the delta/pre-Rad model outperforms the other two Rad score models in terms of predictive performance.

Clinical model and clinical-rad score model

We conducted univariate logistic regression analysis on clinical and Rad indicators and selected those indicators with $P < 0.05$ for multivariate logistic regression analysis. The significant indicators ($P < 0.05$) identified were P53, ypN, Ki67, Post_Rad, and Delta/Pre_Rad. We then calculated the standardized weight for each variable by dividing the absolute value of the regression coefficients by the sum of the absolute values of the coefficients. The results are listed in **Table 4**.

Ki67 = 0.135/(0.135 + 0.201 + 0158 + 1.161 + 4.148) = 0.023

P53 = 0.201/(0.135 + 0.201 + 0158 + 1.161 + 4.148) = 0.034

ypN = 0.158/(0.135 + 0.201 + 0158 + 1.161 + 4.148) = 0.027

Post_Rad = 1.161/(0.135 + 0.201 + 0158 + 1.161 + 4.148) = 0.200

Delta/Pre_Rad = 4.148/(0.135 + 0.201 + 0158 + 1.161 + 4.148) = 0.714

According to the results, the weights of post_Rad and delta/pre_Rad are significantly greater than those of clinical indicators. Among clinical variables, P53 had the greatest weight.

The clinicopathological model developed using the three independent risk indicators demon-

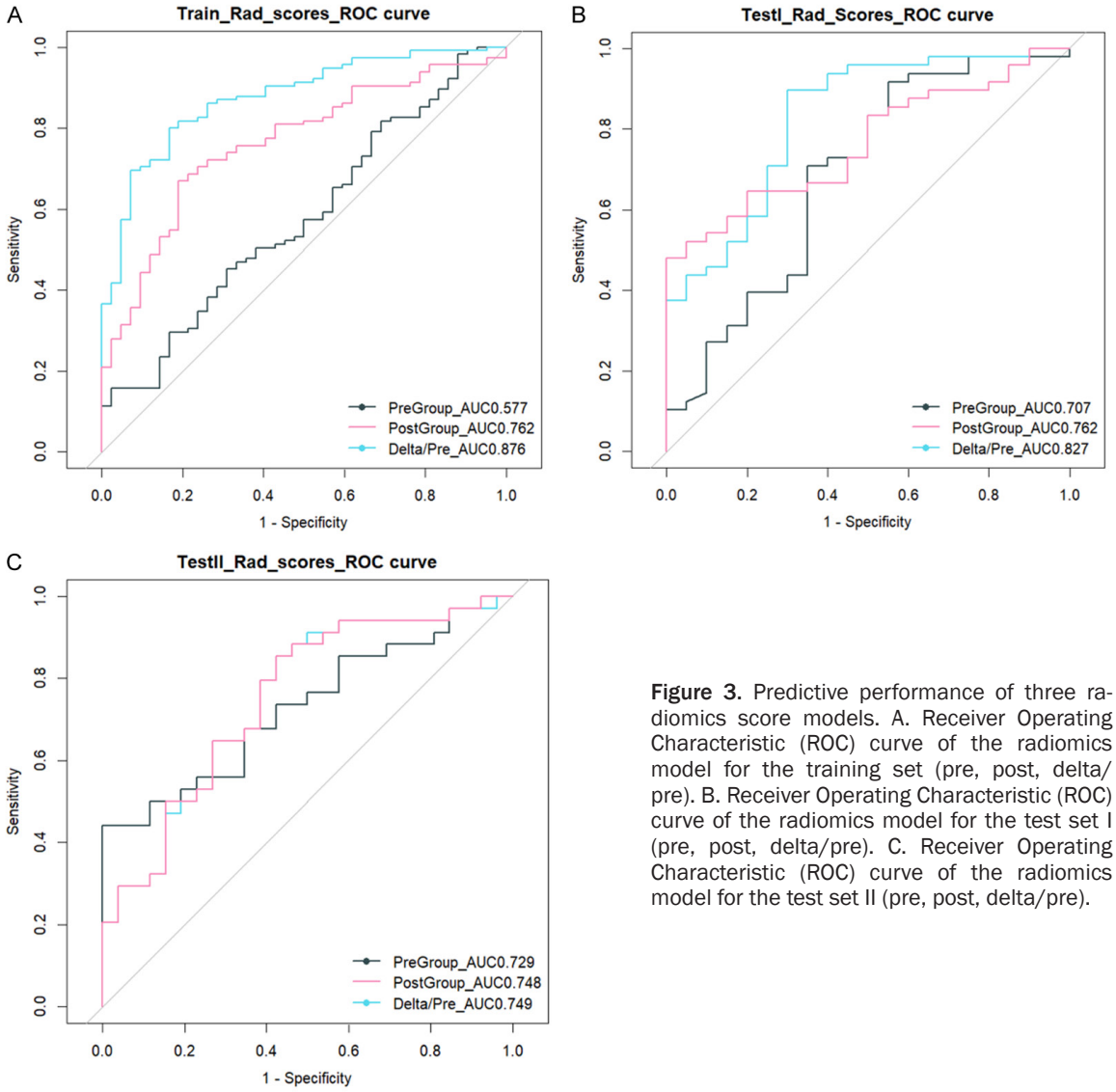

Figure 3. Predictive performance of three radiomics score models. A. Receiver Operating Characteristic (ROC) curve of the radiomics model for the training set (pre, post, delta/pre). B. Receiver Operating Characteristic (ROC) curve of the radiomics model for the test set I (pre, post, delta/pre). C. Receiver Operating Characteristic (ROC) curve of the radiomics model for the test set II (pre, post, delta/pre).

strated AUC of 0.870, 0.876, and 0.844 for the training, test set I, and test set II, respectively (**Figure 4**). Three clinical Rad models were constructed by incorporating features from the clinical model, as well as the pre-Rad, post-Rad, and delta/pre-Rad models. In the training set, these three clinical read models achieved AUC of 0.878, 0.946, and 0.997, respectively (**Figure 4A**). In test set I, the AUC were 0.923, 0.946, and 0.955 (**Figure 4B**). Similarly, in test set II, AUC were 0.865, 0.877, and 0.878, respectively (**Figure 4C**). **Table 3** presents the accuracy, sensitivity, specificity, and corresponding 95% confidence intervals of the clinical Rad models. The experimental results indicated that the clinical Rad model, developed using features from a clinical model, exhibited superior performance. Comparisons between the predicted probabilities from this model and the actual observations are shown in the calibration plots (**Figure 4D-I**).

Finally, a comprehensive Rad score nomogram was developed by incorporating the Rad score, Ki67, ypN, and P53 into the pre-, post-, and delta/pre-groups, respectively (**Figure 6A-C**). **Figure 5** demonstrates that decision curve analysis (DCA) revealed a superior net benefit of clinical intervention across all threshold probabilities compared to treating all or none of the patients within the training set, test set I, and test set II. **Figure 5A** and **5B** show that in test set I and test set II, both the delta/pre-Rad model and the delta/pre-Rad-clinic model pro-

Table 3. The performance of different models was evaluated in training set, test set I and test set II

Models	Train set					Test set I					Test set II				
	AUC	Accuracy	Sensitivity	Specificity	95% CI	AUC	Accuracy	Sensitivity	Specificity	95% CI	AUC	Accuracy	Sensitivity	Specificity	95% CI
Pre-Rad	0.577	0.732	0.452	0.690	0.477-0.677	0.707	0.705	0.895	0.45	0.575-0.839	0.729	0.602	0.460	1	0.729-0.855
Post-Rad	0.762	0.732	0.686	0.809	0.683-0.842	0.762	0.705	0.479	1	0.65-0.875	0.748	0.621	0.852	0.576	0.748-0.874
Delta/Pre-Rad	0.876	0.802	0.800	0.833	0.818-0.933	0.827	0.779	0.895	0.7	0.716-0.938	0.749	0.622	0.853	0.577	0.749-0.875
Clinic	0.870	0.860	0.895	0.690	0.812-0.927	0.876	0.823	0.854	0.75	0.791-0.961	0.796	0.716	0.558	0.885	0.796-0.899
Pre-Rad + Clinic	0.878	0.840	0.826	0.809	0.819-0.937	0.923	0.852	0.833	0.9	0.861-0.984	0.865	0.733	0.960	0.692	0.865-0.960
Post-Rad + clinic	0.949	0.732	0.895	0.952	0.913-0.986	0.946	0.882	0.895	0.9	0.886-0.999	0.877	0.816	0.852	0.769	0.877-0.967
Delta/preRad + clinic	0.997	0.987	0.980	0.952	1	0.955	0.867	0.895	0.9	0.911-0.999	0.878	0.816	0.853	0.770	0.878-0.968

Rad: radiomics; AUC: Area Under Curve; CI: Confidence Interval.

Table 4. Significant clinical features were applied in univariate and multivariate analyses

Variable	Univariate		Multivariate	
	OR (95% CI)	P	OR (95% CI)	P
Ki67				
0				
1	10.359 (3.026-35.462)	0.000	0.135 (0.027-0.678)	0.015
Ker				
0				
1	4.636	0.000		
P53				
0				
1	11.922	0.000	0.201 (0.051-0.79)	0.022
ypN				
0				
1	4.478	0.001	0.158 (0.045-0.552)	0.004
Pre_Rad	1.038	0.069		
Post_Rad	5.941	0.000	1.161 (1.053-1.279)	0.003
Delta/Pre	1.131	0.000	4.148 (1.848-9.308)	0.001

Ker: Keratin expression level; Ki67: Ki67 expression level; P53: P53 mutation status; ypN: lymph node after neoadjuvant therapy; Rad: radiomics; OR: Odds ratio; CI: Confidence Interval.

vide a greater net benefit compared to the other models at the same probability value. **Figure 5C** and **5D** compare the delta/pre-Rad, delta/pre-Rad-clinic, and fusion models, showing these three models offer the similar net benefit. The delta/pre-Rad model is slightly higher than the other two. The DCA curve for set II is similar to that of set I, indicating the model's strong generalization ability.

Discussion

As neoadjuvant therapy for ESCC has entered the era of immunotherapy, the combination of NIC has increasingly become a focal point for LAESCC. The interaction between immune checkpoint inhibitors and PD-L1 on tumor cells promotes extensive infiltration of antitumor immune cells, particularly CD8+ T cells. Although immune cells can phagocytize tumor cells, the extent of the lesion volume varies. Therefore, changes in histological type may be more informative than changes in morphological anatomy for assessing the efficacy of immunotherapy.

Several studies have shown that lesions may not shrink and may even enlarge during immunotherapy. However, subsequent postoperative pathology revealed regression of tumor cells accompanied by infiltration of inflammatory, immune, or fibroblast cells. Therefore, conventional imaging techniques based solely on volume alterations are inadequate for accurately assessing changes in lesional tissue composition, which may lead to misdiagnoses. The delta/pre-Rad model developed in our study exhibited high AUC values in the training set (AUC = 0.876) and two independent test sets (AUC = 0.827 and AUC = 0.749), indicating its reliability for predicting NIC response in patients with LAESCC.

In a previous study conducted on 95 patients with LAESCC, eight radiomics features were utilized to develop a machine learning model for predicting the PCR of NIC. The AUC values obtained were 0.77 and 0.85 for the training set (66 patients) and test set (29 patients), respectively [14]. Another study focused on predicting NIC-induced PCR in 64 patients with LAESCC, in which a model incorporating five selected radiomics features demonstrated an accuracy of 0.796 in distinguishing different degrees of tumor regression within the test cohort [15].

Compared to two previous studies, both of which utilized a considerable number of features for constructing the learning model, our delta/pre-model reduced overfitting and enhanced the generalization ability of the mo-

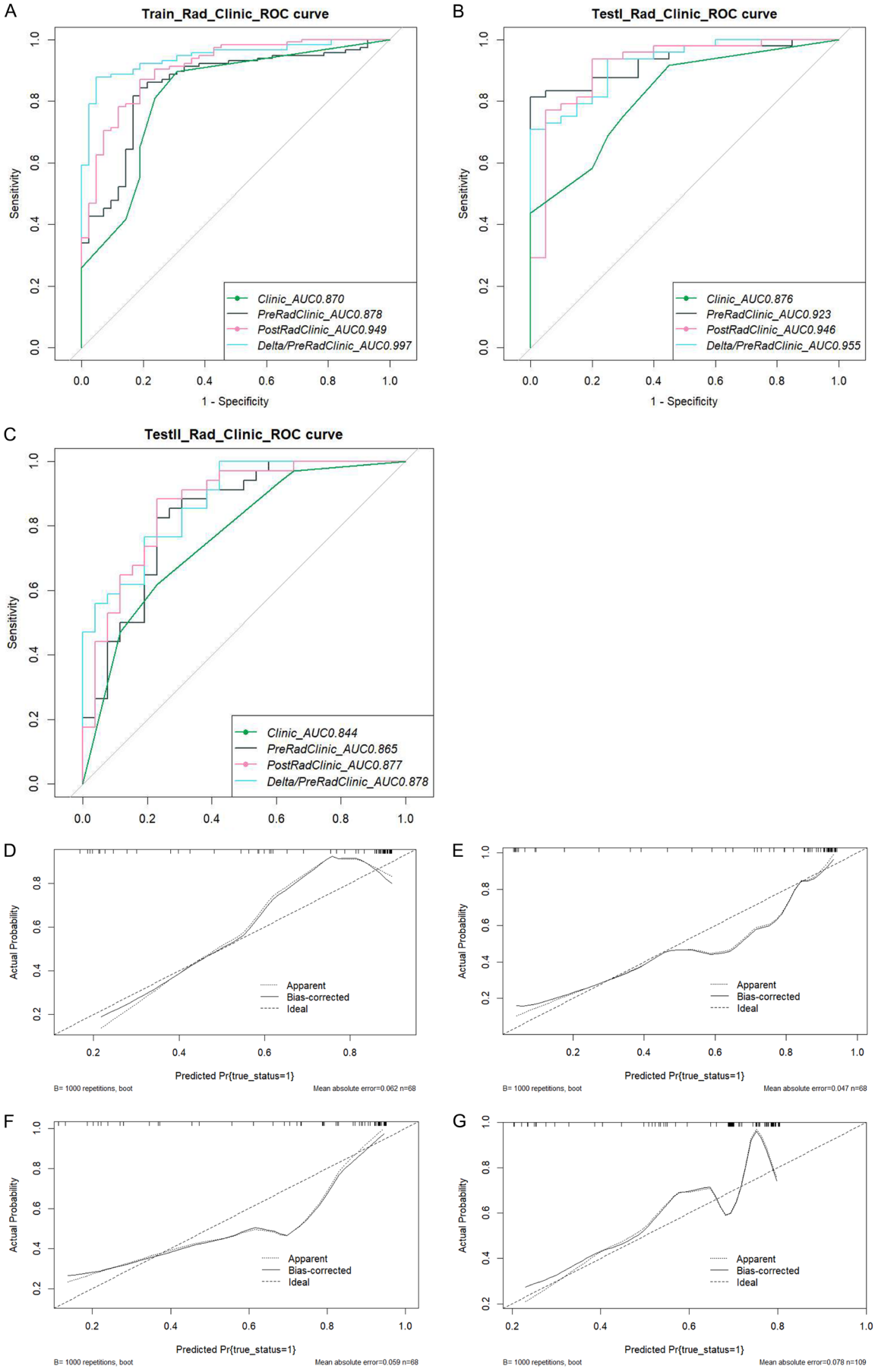
A
Train_Rad_Clinic_ROC curve
Sensitivity
1 - Specificity
Clinic_AUC0.870
PreRadClinic_AUC0.878
PostRadClinic_AUC0.949
Delta/PreRadClinic_AUC0.997
B
Testl_Rad_Clinic_ROC curve
Sensitivity
1 - Specificity
Clinic_AUC0.876
PreRadClinic_AUC0.923
PostRadClinic_AUC0.946
Delta/PreRadClinic_AUC0.955
C
TestII_Rad_Clinic_ROC curve
Sensitivity
Clinic_AUC0.844
PreRadClinic_AUC0.865
PostRadClinic_AUC0.877
Delta/PreRadClinic_AUC0.878
D
Actual Probability
Apparent
Bias-corrected
Ideal
Predicted Pr{true_status=1}
B= 1000 repetitions, boot
Mean absolute error=0.062 n=68
E
Actual Probability
Apparent
Bias-corrected
Ideal
Predicted Pr{true_status=1}
B= 1000 repetitions, boot
Mean absolute error=0.047 n=68
F
Actual Probability
Apparent
Bias-corrected
Ideal
Predicted Pr{true_status=1}
B= 1000 repetitions, boot
Mean absolute error=0.059 n=68
G
Actual Probability
Apparent
Bias-corrected
Ideal
Predicted Pr{true_status=1}
B= 1000 repetitions, boot
Mean absolute error=0.078 n=109

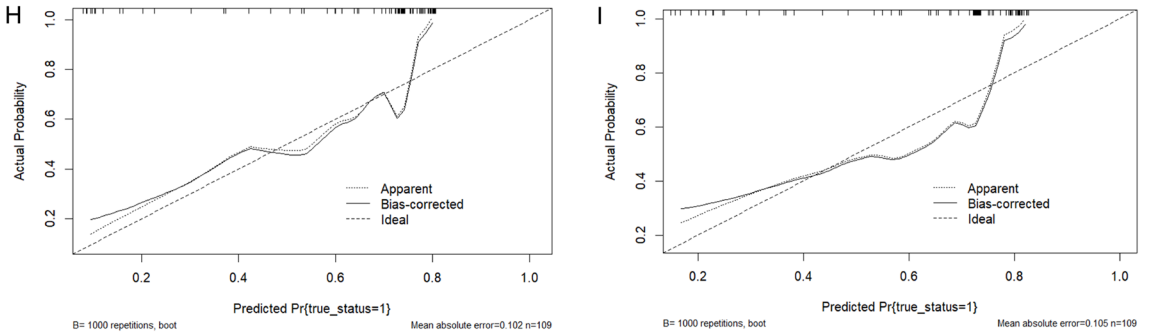

Figure 4. Predictive performance of three Rad-clinical models. A-C. Receiver operating characteristic (ROC) curves of Rad-clinical score models in the training set, test set I, and test II. D-F. The calibration curve uses test set I data to validate the performance of three models (Pre, post, delta/pre). G-I. The calibration curve uses test set II data to validate the performance of the three models compared with trained models in the training set.

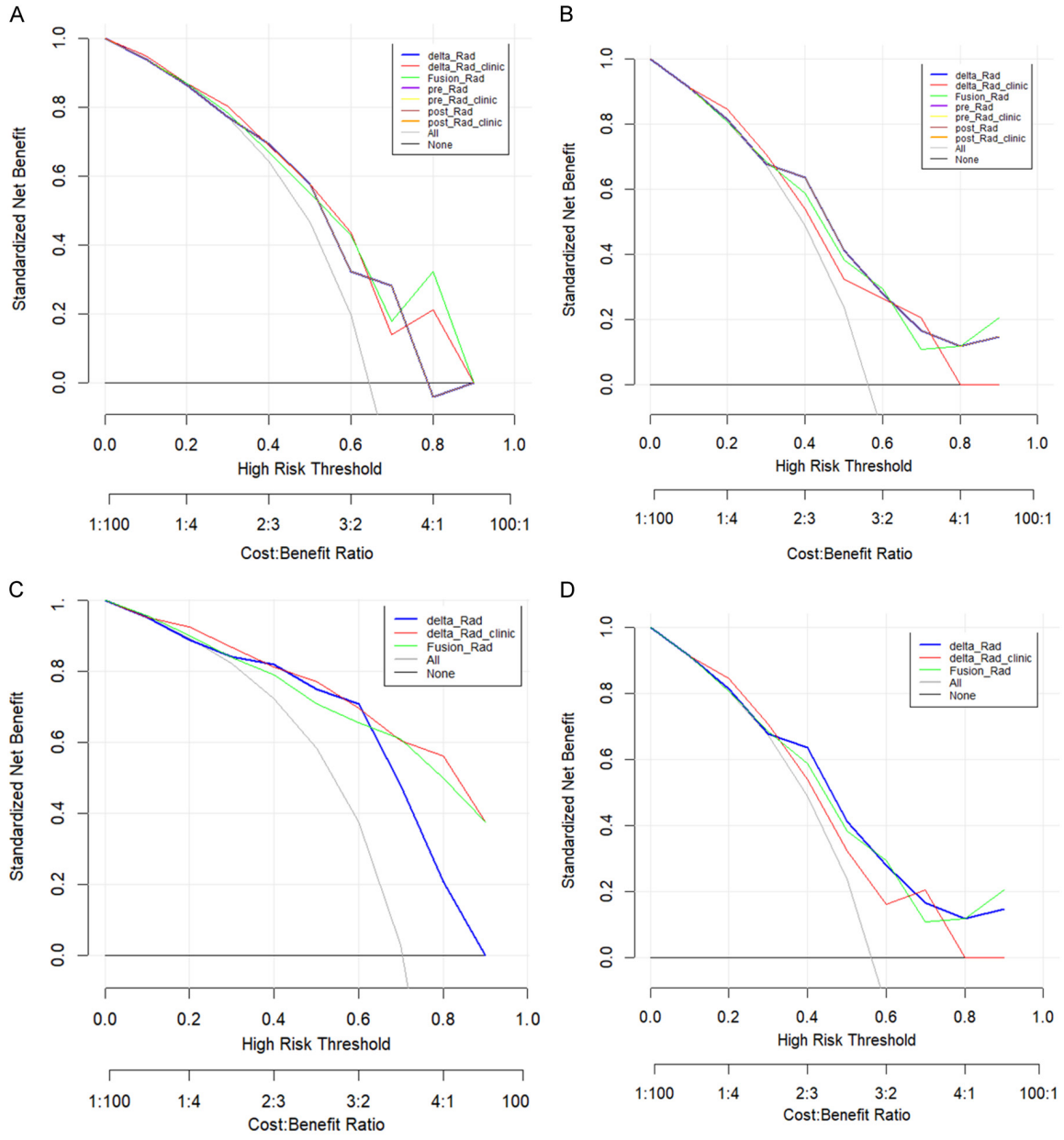

Figure 5. A. DCA of delta/pre_Rad,delta/pre_Rad_clinic,Fusion Rad(pre_Rad,post_Rad,delta/pre_Rad),pre_Rad,pre_Rad_clinic,post_Rad,post_Rad_clinic model in the test set I. B. DCA of delta/pre_Rad,delta/pre_Rad_clinic,FusionRad(pre_Rad,post_Rad,delta/pre_Rad),pre_Rad,pre_Rad_clinic,post_Rad,post_Rad_clinic model in the test set II. C. DCA of delta/pre_Rad,delta/pre_Rad_clinic,Fusion Rad in the test set I. D. DCA of delta/pre_Rad,delta/pre_Rad_clinic,Fusion Radin the test II.

del. Additionally, our study had a significantly larger sample size (225 + 60) than previous studies (95 vs. 64) [15, 16]. In addition to internal validation, our model demonstrated external validation results, further enhancing its generalizability. Neoadjuvant therapy for esophageal cancer encompasses various methods, and the commonly used approaches in clinical practice include neoadjuvant radiotherapy and nRCT. Immunotherapy has traditionally been employed as the second-line treatment for advanced esophageal cancer; however, NIC has gradually emerged as an adjunctive therapy in recent years. The successfully published Keynote-590, CheckMate-648, and ESCORT-1st studies demonstrated that pembrolizumab significantly improves overall survival in the first-line treatment of advanced esophageal cancer, regardless of the histological type [17-19]. These findings reaffirm the importance of immunotherapy as a first-line treatment for patients with advanced esophageal cancer. Consequently, research on the radiomic evaluation of the efficacy of neoadjuvant chemotherapy combined with immunotherapy is limited.

In addition, a retrospective study of 54 patients with LAESCC treated with PD-1 inhibitors combined with chemotherapy who successfully achieved PCR demonstrated significantly higher body mass index levels than those without PCR [20]. Furthermore, a previous study utilized microscopic venous invasion as a prognostic predictor in 143 patients who received neoadjuvant chemotherapy followed by surgery for ESCC without neoadjuvant immunotherapy [21]. However, in our study involving 225 patients, we identified several clinical factors, including R0 section status, Ker, LVI, PNI, Ki67 expression level, P53 mutation status, ypN stage, and N-counts that showed statistical significance in predicting PCR after neoadjuvant induction chemotherapy for LAESCC. Additionally, the predictive values of R0 section status, LVI, Ki67, ypN, and P53 were validated in independent test set I (n = 68), while LVI, PNI, Ki67, P53, and N-counts were statistically significant in an external validation set (n = 60). After univariate and multivariate analyses, we obtained the clinical variables ypN, P53, and Ki67 with $P < 0.05$. These significant clinical factors were incorporated into a clinical model that achieved AUC values of 0.870, 0.876, and 0.844 for the training and two independent test sets, respectively.

We developed seven machine learning models to predict the efficacy of neoadjuvant chemotherapy combined with immunotherapy for LAESCC: pre-Rad, post-Rad, delta/pre-Rad, pre-Rad-clinic, post-Rad-clinic, delta/pre-Rad-clinic, and Fusion models. Among these models, the delta/pre-Rad fusion clinical model demonstrated superior performance, with AUC values of 0.997, 0.955, and 0.878, emerging as the most effective model.

Our study revealed that the original shape flatness (representing the shape of the original feature) and original first-order maximum (indicating the first-order wavelet features) were significantly associated with LAESCC. Flatness, a characteristic of tumor morphology, reflects variations in different tumor regions, suggesting irregular and lobulated edges in the lesion. Fine and short spicules, prickly projections, and serrated changes were observed at the periphery of the lesions. The original first-order maximum represents the highest gray scale value within the ROIs, implying a potential link between tumor regression and areas of necrosis [22]. Previous studies have demonstrated that radiomic features can serve as phenotypes for esophageal cancer; however, these studies have primarily focused on T staging, treatment response evaluation, and prognosis [23]. Furthermore, a considerable exploration of the biological mechanisms underlying TRG and its radiomic features is required.

In this study, DCA was performed using the pre-Rad, post-Rad, delta/pre-Rad, pre-Rad-clinic, post-Rad-clinic, delta/pre-Rad-clinic, and fusion models. The delta/pre-Rad, delta/pre-Rad-clinic and Fusion model all demonstrated

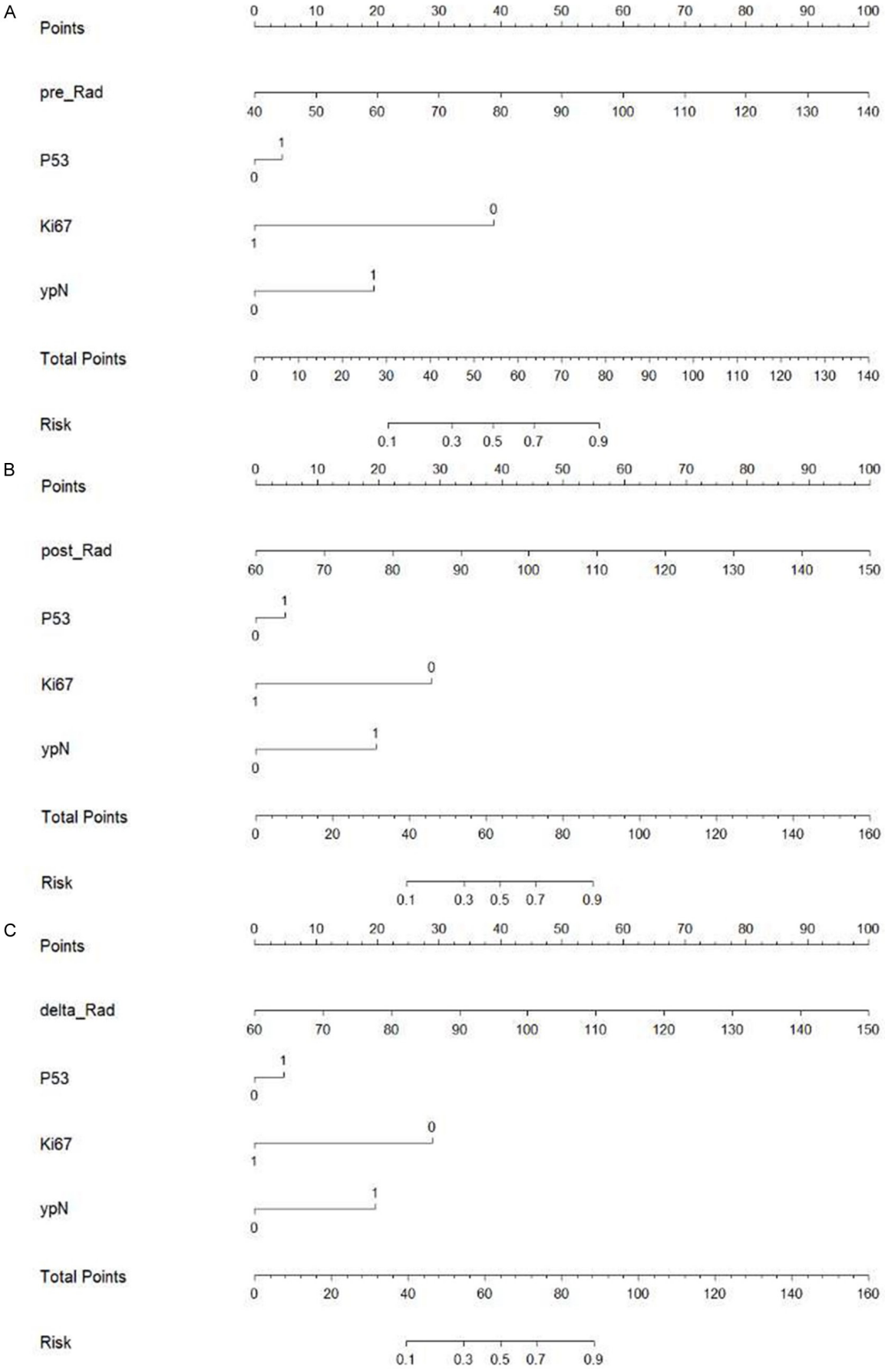
A
Points
0 10 20 30 40 50 60 70 80 90 100
pre_Rad
40 50 60 70 80 90 100 110 120 130 140
P53
1
0
Ki67
0
1
ypN
1
0
Total Points
0 10 20 30 40 50 60 70 80 90 100 110 120 130 140
Risk
0.1 0.3 0.5 0.7 0.9
B
Points
0 10 20 30 40 50 60 70 80 90 100
post_Rad
60 70 80 90 100 110 120 130 140 150
P53
1
0
Ki67
0
1
ypN
1
0
Total Points
0 20 40 60 80 100 120 140 160
Risk
0.1 0.3 0.5 0.7 0.9
C
Points
0 10 20 30 40 50 60 70 80 90 100
delta_Rad
60 70 80 90 100 110 120 130 140 150
P53
1
0
Ki67
0
1
ypN
1
0
Total Points
0 20 40 60 80 100 120 140 160
Risk
0.1 0.3 0.5 0.7 0.9

Figure 6. The nomogram of radiomics prediction models. A-C. The nomogram obtained from the pre Rad,post Rad,delta/pre Rad model combined with Ki67, Lym, and P53.

a potential clinical utility, with the delta/pre-Rad model being the most powerful. Decision-makers can choose the most appropriate model based on the clinical situation or threshold.

For patients with LAESCC, this model has the potential to identify nonresponders to NIC before surgery, thereby improving therapeutic accuracy and reducing unnecessary treatment costs. Radiotherapy or alternative methods should be promptly considered in these patients. Additionally, radiomic features serve as noninvasive markers that comprehensively capture the heterogeneity of lesions. Traditional gastroscopic pathological biopsy and even postoperative general pathology offer limited tumor tissue samples for examination, potentially compromising the diversity of the pathological results. In conclusion, we recommend delta-/pre-enhanced CT-based radiomics combined with clinical models to display the total score of each patient, offering guidance to clinicians before surgery, and guiding the consecutive treatment of patients.

Acknowledgements

We acknowledge the work of all the authors. Final approval of the manuscript was based on the consensus of all the authors.

Disclosure of conflict of interest

None.

Address correspondence to: Shuangqing Chen, Department of Radiology, The Affiliated Suzhou Hospital of Nanjing Medical University, Suzhou Municipal Hospital, Gusu School, Nanjing Medical University, Suzhou 215001, Jiangsu, China. E-mail: sznaonao@163.com

References

[1] Yin J, Lin S, Fang Y, Jiao H, Chen Z, Tang H, Gu J, Zhang S, Sun L, Li Y, Han Y, Chen Q, Chen H, Li Z and Tan L. Neoadjuvant therapy with immunoagent (nivolumab) or placebo plus chemotherapy followed by surgery and adjuvant treatment in subjects with resectable esophageal squamous cell carcinoma: study protocol of a randomized, multicenter, double blind, phase II trial (NATION-2203 trial). J Thorac Dis 2023; 15: 718-730.

[2] Strong VE, D'Amico TA, Kleinberg L and Ajani J. Impact of the 7th Edition AJCC staging classification on the NCCN clinical practice guidelines in oncology for gastric and esophageal cancers. J Natl Compr Canc Netw 2013; 11: 60-66.

[3] Xu J, Yan C, Li Z, Cao Y, Duan H and Ke S. Efficacy and safety of neoadjuvant chemoimmunotherapy in resectable esophageal squamous cell carcinoma: a meta-analysis. Ann Surg Oncol 2023; 30: 1597-1613.

[4] Tang H, Wang H, Fang Y, Zhu JY, Yin J, Shen YX, Zeng ZC, Jiang DX, Hou YY, Du M, Lian CH, Zhao Q, Jiang HJ, Gong L, Li ZG, Liu J, Xie DY, Li WF, Chen C, Zheng B, Chen KN, Dai L, Liao YD, Li K, Li HC, Zhao NQ and Tan LJ. Neoadjuvant chemoradiotherapy versus neoadjuvant chemotherapy followed by minimally invasive esophagectomy for locally advanced esophageal squamous cell carcinoma: a prospective multicenter randomized clinical trial. Ann Oncol 2023; 34: 163-172.

[5] Kitasaki N, Hamai Y, Emi M, Kurokawa T, Yoshikawa T, Hirohata R, Ohsawa M and Okada M. Prognostic factors for patients with esophageal squamous cell carcinoma after neoadjuvant chemotherapy followed by surgery. In Vivo 2022; 36: 2852-2860.

[6] Park SY, Hong MH, Kim HR, Lee CG, Cho JH, Cho BC and Kim DJ. The feasibility and safety of radical esophagectomy in patients receiving neoadjuvant chemoradiotherapy with pembrolizumab for esophageal squamous cell carcinoma. J Thorac Dis 2020; 12: 6426-6434.

[7] Zheng Y, Li C, Yu B, Zhao S, Li J, Chen X and Li H. Preoperative pembrolizumab combined with chemoradiotherapy for esophageal squamous cell carcinoma: trial design. JTCVS Open 2022; 9: 293-299.

[8] He W, Wang C, Li C, Nie X, Li H, Li J, Zhao N, Chen H, Miao X, Han Y, Peng L and Leng X. The efficacy and safety of neoadjuvant immunotherapy in resectable locally advanced esophageal squamous cell carcinoma: a systematic review and meta-analysis. Front Immunol 2023; 14: 1118902.

[9] Helminen O, Melkko J, Saarnio J, Sihvo E, Kuopio T, Ohtonen P, Kauppila JH, Karttunen TJ and Huhta H. Predictive value of p53, Ki67 and TLR5 in neoplastic progression of Barrett's esophagus: a matched case-control study. Virchows Arch 2022; 481: 467-476.

[10] Wu TT, Chirieac LR, Abraham SC, Krasinskas AM, Wang H, Rashid A, Correa AM, Hofstetter WL, Ajani JA and Swisher SG. Excellent interobserver agreement on grading the extent of residual carcinoma after preoperative chemoradiation in esophageal and esophagogastric junction carcinoma: a reliable predictor for patient outcome. Am J Surg Pathol 2007; 31: 58-64.

[11] Karamitopoulou E, Thies S, Zlobec I, Ott K, Feith M, Slotta-Huspenina J, Lordick F, Becker K and Langer R. Assessment of tumor regression of esophageal adenocarcinomas after neoadjuvant chemotherapy: comparison of 2 commonly used scoring approaches. Am J Surg Pathol 2014; 38: 1551-1556.

[12] Japan Esophageal Society. Japanese classification of esophageal cancer, 11th edition: part I. Esophagus 2017; 14: 1-36.

[13] Sikkema M, Kerkhof M, Steyerberg EW, Kusters JG, van Strien PM, Looman CW, van Dekken H, Siersema PD and Kuipers EJ. Aneuploidy and overexpression of Ki67 and p53 as markers for neoplastic progression in Barrett's esophagus: a case-control study. Am J Gastroenterol 2009; 104: 2673-2680.

[14] Li K, Li Y, Wang Z, Huang C, Sun S, Liu X, Fan W, Zhang G and Li X. Delta-radiomics based on CT predicts pathologic complete response in ESCC treated with neoadjuvant immunochemotherapy and surgery. Front Oncol 2023; 13: 1131883.

[15] Zhu Y, Yao W, Xu BC, Lei YY, Guo QK, Liu LZ, Li HJ, Xu M, Yan J, Chang DD, Feng ST and Zhu ZH. Predicting response to immunotherapy plus chemotherapy in patients with esophageal squamous cell carcinoma using non-invasive radiomic biomarkers. BMC Cancer 2021; 21: 1167.

[16] Li K, Li Y, Wang Z, Huang C, Sun S, Liu X, Fan W, Zhang G and Li X. Delta-radiomics based on CT predicts pathologic complete response in ESCC treated with neoadjuvant immunochemotherapy and surgery. Front Oncol 2023; 13: 1131883.

[17] Sun JM, Shen L, Shah MA, Enzinger P, Adenis A, Doi T, Kojima T, Metges JP, Li Z, Kim SB, Cho BC, Mansoor W, Li SH, Sunpaweravong P, Maqueda MA, Goekkurt E, Hara H, Antunes L, Fountzilas C, Tsuji A, Oliden VC, Liu Q, Shah S, Bhagia P and Kato K. Pembrolizumab plus chemotherapy versus chemotherapy alone for first-line treatment of advanced oesophageal cancer (KEYNOTE-590): a randomised, placebo-controlled, phase 3 study. Lancet 2021; 398: 759-771.

[18] Kato K, Shah MA, Enzinger P, Bennouna J, Shen L, Adenis A, Sun JM, Cho BC, Özgüroğlu M, Kojima T, Kostorov V, Hierro C, Zhu Y, McLean LA, Shah S and Doi T. KEYNOTE-590: phase III study of first-line chemotherapy with or without pembrolizumab for advanced esophageal cancer. Future Oncol 2019; 15: 1057-1066.

[19] Luo H, Lu J, Bai Y, Mao T, Wang J, Fan Q, Zhang Y, Zhao K, Chen Z, Gao S, Li J, Fu Z, Gu K, Liu Z, Wu L, Zhang X, Feng J, Niu Z, Ba Y, Zhang H, Liu Y, Zhang L, Min X, Huang J, Cheng Y, Wang D, Shen Y, Yang Q, Zou J and Xu RH. Effect of camrelizumab vs placebo added to chemotherapy on survival and progression-free survival in patients with advanced or metastatic esophageal squamous cell carcinoma: the ESCORT-1st randomized clinical trial. JAMA 2021; 326: 916-925.

[20] Chen W, Li D, Bian X, Wu Y, Xu M, Wu M and Tao M. Peripheral blood markers predictive of progression-free survival in advanced esophageal squamous cell carcinoma patients treated with PD-1 inhibitors plus chemotherapy as first-line therapy. Nutr Cancer 2023; 75: 207-218.

[21] Tanishima Y, Takahashi K, Nishikawa K, Ishikawa Y, Yuda M, Tanaka Y, Matsumoto A, Yano F and Eto K. Microscopic venous invasion is a predictor of prognosis in patients with esophageal squamous cell carcinoma undergoing ineffective neoadjuvant chemotherapy and surgery. Esophagus 2023; 20: 651-659.

[22] Dahlsgaard-Wallenius SE, Hildebrandt MG, Johansen A, Vilstrup MH, Petersen H, Gerke O, Høilund-Carlsen PF, Morsing A and Andersen TL. Hybrid PET/MRI in non-small cell lung cancer (NSCLC) and lung nodules-a literature review. Eur J Nucl Med Mol Imaging 2021; 48: 584-591.

[23] Wen Q, Yang Z, Zhu J, Qiu Q, Dai H, Feng A and Xing L. Pretreatment CT-based radiomics signature as a potential imaging biomarker for predicting the expression of PD-L1 and CD8+TILs in ESCC. Onco Targets Ther 2020; 13: 12003-12013.

Supplementary Material 1

The SOMATOM Force system (Siemens) was employed for CT scanning in hospital A. The tube voltage was configured within the range of 80-140 kV, while the tube current ranged from 50-300 mA. The detector collimation was set at a dimension of 64 × 1.2 mm, and both the slice thickness and spacing were standardized at 5 mm.

The Revolution APEX system (GE) was employed for CT scanning in hospital B. The tube voltage was set between 80-140 kV, with the tube current between 50 and 300 mA. The detector collimation was set at a dimension of 64 × 1.2 mm, and both the slice thickness and spacing were standardized at 5 mm.

Supplementary Material 2

There were two features for the pre group, 10 for the post group, and 11 for delta/pre group. Their coefficients were determined by Binary Logistic Regression.

The results of pre group:

feature Apre ‘original_shape_Flatness’_0.0392,

feature Bpre ‘original_firstorder_Maximum’-0.6046.

The results of post group:

feature Apost ‘original_shape_SurfaceVolumeRatio’-1.0750,

feature Bpost ‘original_firstorder_TotalEnergy’_14.4622,

feature Cpost ‘original_firstorder_Energy’_17.5317,

feature Dpost ‘original_firstorder_Median’_2.2928,

feature Epost ‘original_shape_MeshVolume’_-9.4188,

feature Fpost ‘original_shape_VoxelVolume’_21.3544,

feature Gpost ‘original_firstorder_Mean’_-1.7655,

feature Hpost ‘diagnostics_Mask_original_VoxelNum’_-11.5045,

feature Ipost ‘original_shape_Sphericity’_1.6210,

feature Jpost ‘original_glszm_LargeAreaEmphasis’_0.2738.

The results of the delta/pre group:

feature Adelta/pre ‘original_glszm_gray_level_variance’_0.2391,

feature Bdelta/pre ‘original_firstorder_range’_-0.1353,

feature Cdelta/pre ‘original_glrlm_long_run_low_gray_level_emphasis’_0.6571,

feature Ddelta/pre ‘original_gldm_large_dependence_low_gray_level_emphasis’_0.0016,

feature Edelta/pre ‘original_shape_sphericity’_-0.6673,

feature Fdelta/pre ‘original_gldm_small_dependence_low_gray_level_emphasis’_-0.4740,

feature Gdelta/pre ‘original_glcm_correlation’_0.0286,

feature Hdelta/pre ‘original_glszm_high_gray_level_zone_emphasis’_1.1023,

feature Idelta/pre ‘original_glrlm_short_run_high_gray_level_emphasis’_0.2865 3.5625,

feature Jdelta/pre ‘original_glcm_mcc’_-0.1367,

feature Kdelta/pre ‘original_glcm_imc1’_-0.4842.

Supplementary Material 3

The simplified image presented in **Figure 2**, along with the original image that is not included in this article.

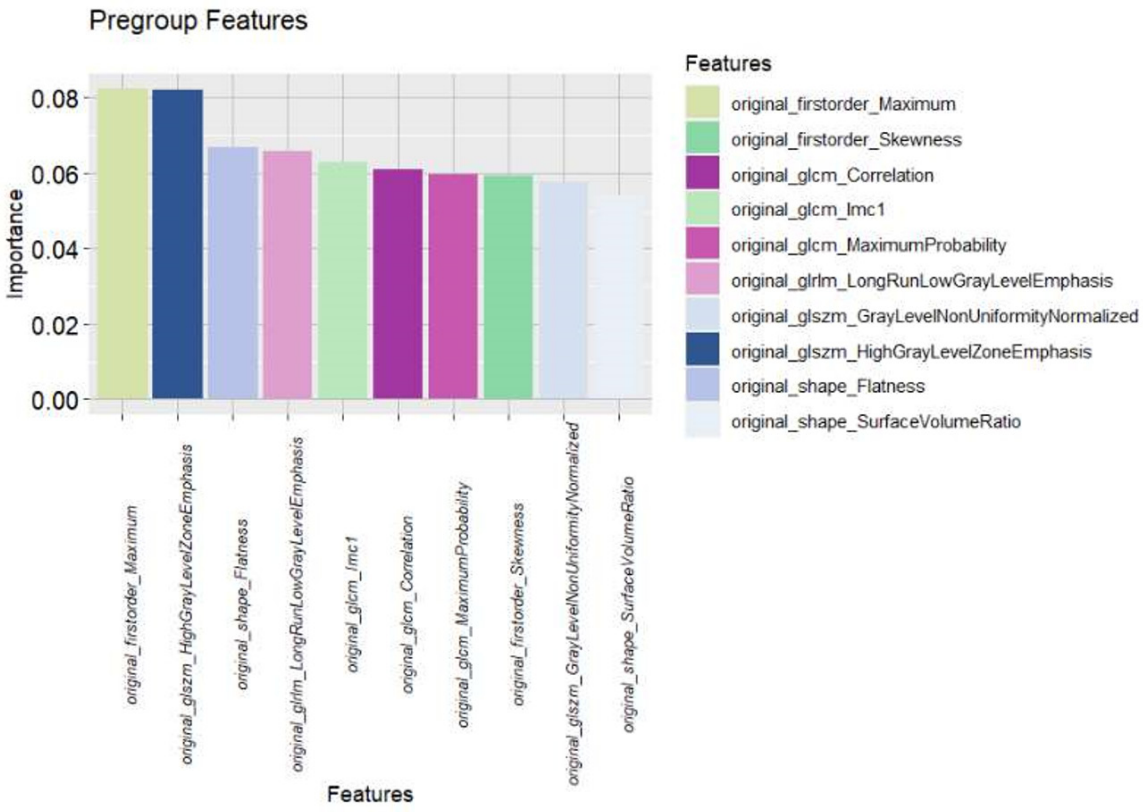

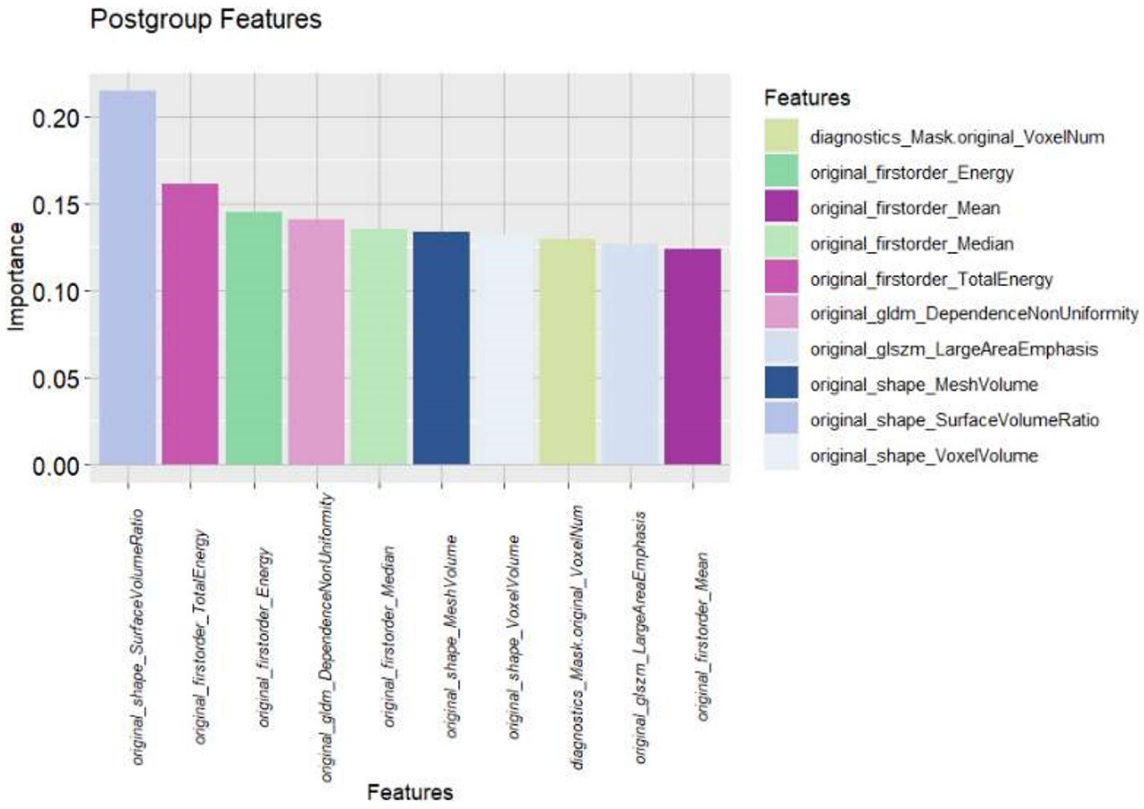
Postgroup Features
Importance
0.20
0.15
0.10
0.05
0.00
original_shape_SurfaceVolumeRatio
original_firstorder_TotalEnergy
original_firstorder_Energy
original_gldm_DependenceNonUniformity
original_firstorder_Median
original_shape_MeshVolume
original_shape_VoxelVolume
diagnostics_Mask.original_VoxelNum
original_glszm_LargeAreaEmphasis
original_firstorder_Mean
Features
Features
diagnostics_Mask.original_VoxelNum
original_firstorder_Energy
original_firstorder_Mean
original_firstorder_Median
original_firstorder_TotalEnergy
original_gldm_DependenceNonUniformity
original_glszm_LargeAreaEmphasis
original_shape_MeshVolume
original_shape_SurfaceVolumeRatio
original_shape_VoxelVolume

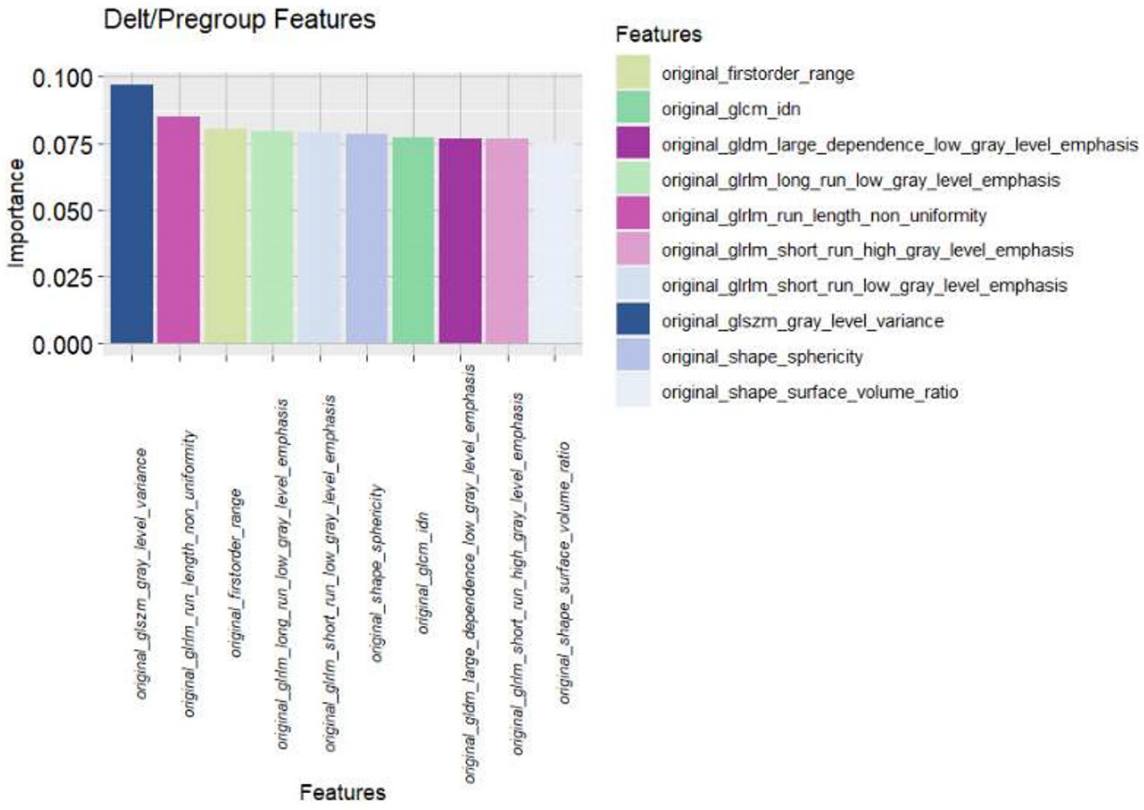
Delt/Pregroup Features
Importance
0.100
0.075
0.050
0.025
0.000
original_glszm_gray_level_variance
original_glrlm_run_length_non_uniformity
original_firstorder_range
original_glrlm_long_run_low_gray_level_emphasis
original_glrlm_short_run_low_gray_level_emphasis
original_shape_sphericity
original_glcm_idn
original_gldm_large_dependence_low_gray_level_emphasis
original_glrlm_short_run_high_gray_level_emphasis
original_shape_surface_volume_ratio
Features
Features
original_firstorder_range
original_glcm_idn
original_gldm_large_dependence_low_gray_level_emphasis
original_glrlm_long_run_low_gray_level_emphasis
original_glrlm_run_length_non_uniformity
original_glrlm_short_run_high_gray_level_emphasis
original_glrlm_short_run_low_gray_level_emphasis
original_glszm_gray_level_variance
original_shape_sphericity
original_shape_surface_volume_ratio